

Ceramic On-Demand Extrusion of ZrB₂-SiC Microchannels for Ultra High-Temperature Compact Heat Exchanger

Abid Hasan Rafi¹, Marharyta Lakusta², Vincenzo Anthony¹, Grace Basler², Sophie Grier²,
Lauren Moeller², David Lipke², Jeremy Lee Watts², Greg Hilmas², Ming C Leu¹

¹ Department of Mechanical and Aerospace Engineering, Missouri University of Science and Technology, Rolla, Missouri

² Department of Materials Science and Engineering, Missouri University of Science and Technology, Rolla, Missouri

Abstract

Ceramic On-Demand Extrusion (CODE) is a paste extrusion based additive manufacturing process that has been developed for the fabrication of dense ceramic components. This paper presents a study of using the CODE process to build microchannels with ZrB₂-SiC aqueous paste for the fabrication of an ultra-high-temperature compact heat exchanger (CHE). The aqueous paste is developed from ZrB₂ and SiC (70/30 vol%) powders to possess properties suitable for the extrusion process. The performance and properties of the microchannels are tested for use in the CHE, which features a large heat transfer area to volume ratio and has potential applications in aero-engines, microturbines, etc., as well as high-efficiency power generation systems.

Keywords: Additive Manufacturing, Ceramic On-Demand Extrusion, High-temperature Ceramic, Compact Heat Exchanger, Microchannel, Paste Extrusion

1. Introduction

The supercritical carbon dioxide (sCO₂) Brayton cycle has gotten a lot of interest in recent years for use in energy applications like waste heat recovery [1,2], solar-thermal systems [3-4], fuel cells [5,6], coal power [7-9], geothermal power [10], and nuclear power [11,12] because of its high efficiency, small footprint, and simple layout. sCO₂ has a higher diffusivity, lower viscosity, and lower surface tension than liquid CO₂. For similar turbine intake temperatures, several studies have found that sCO₂ Brayton power cycles have higher cycle efficiency than traditional Rankine and gas Brayton power cycles [13]. The combination of performing the cycle in the supercritical state, lower operating pressure ratios, and relatively high turbine exit temperatures allows for extensive recuperation, resulting in a highly efficient and compact power block. Compact microchannel heat exchangers are commonly utilized in sCO₂ power plants, among the different heat exchanger layouts available.

The heat exchanger is an effective device to increase the energy efficiency of a process by recovering the wasted energy as much as possible, by transferring heat between two or more fluids for both heating and cooling industrial processes. With the rising effort to make sCO₂ cycle more energy efficient, a new generation of heat exchangers is needed that can give greater performance while keeping the heat exchanger's cost and size to minimum. Increasing the surface area to volume ratio of heat exchangers by using mini and micro channels is one way to improve heat transfer performance.

Nowadays, compact heat exchangers (CHEs) are widely used for the heat exchanging process and provide benefits over conventional (shell-and-tube) heat exchangers in compactness, large surface area per volume ratio, and low temperature difference. CHEs are distinguished by their relatively high area density. The ratio of heat transfer surface to heat exchanger volume is known as area density. According to Shah [14], the compact heat exchanger has a surface area density more than $400 \text{ m}^2/\text{m}^3$ for liquid heat exchangers whereas the surface area density of a typical process industry shell-and-tube heat exchanger is less than $100 \text{ m}^2/\text{m}^3$ [15]. Human lungs are one of the smallest heat exchangers, with an area density of roughly $17,500 \text{ m}^2/\text{m}^3$, or equivalent to about 0.19 mm diameter tubes [16]. The need to reduce energy consumption, capital investment, and component adaptability has sped up research on CHEs and their applications in a variety of fields, particularly in high-temperature services. The high aspect ratios, thin walls, and tight spacing lead to complex geometries that can be difficult to achieve for manufacturers. As well, the selection of a material compatible with high-temperature applications is also a challenge.

Ceramic materials have a number of advantages over typical metallic materials in CHE construction, including high-temperature stability, low material cost, and superior corrosion resistance [16]. The operating temperatures of ceramic based CHEs are significantly higher than those of typical metallic alloys. Ceramic CHEs provide excellent fouling resistance, corrosion resistance, and chemical erosion resistance at high working temperatures. Zirconium diboride is an early transition metal boride that has very high melting points ($>3000^\circ\text{C}$) and is classified as an ultra-high temperature ceramic (UHTC). ZrB_2 has the lowest theoretical density ($6.09 \text{ g}/\text{cm}^3$) in the family of ultra-high temperature ceramics as well as a unique combination of properties including high strength, hardness, electrical and thermal conductivities, good oxidation, and resistance to chemical attack, which makes ZrB_2 -based ceramics an attractive candidate for aerospace applications such as leading edges and thermal protection systems for reusable atmospheric re-entry vehicles, hypersonic flight vehicles, and rocket propulsion systems as well as components for corrosive environments and wear-resistant applications [17,18].

As a refractory boride, ZrB_2 oxidizes when exposed to air at elevated temperatures. In addition, because of its strong covalent bonding and low self-diffusion coefficient, SiC particles are added to monolithic ZrB_2 to increase the densification, mechanical properties, and oxidation resistance. In this study, ZrB_2 ceramics containing 10, 20, and 30 vol% SiC particulates were prepared and the four-point bend strength, fracture toughness, elastic modulus, and hardness were measured [17]. The measured data are given in Table 1. Though the elastic modulus and hardness did not change much with the content of SiC, a substantial increase in strength and toughness was noticeable as SiC content increased, with the relative density maintained at $\sim 99\%$.

Table 1: Properties of ZrB_2 -SiC ceramics

SiC content (vol%)	Relative Density (%)	Modulus (GPa)	Hardness (GPa)	Strength (MPa)	Toughness ($\text{MPa} \cdot \text{m}^{0.5}$)
0	99.8	489	23 ± 0.9	565 ± 53	3.5 ± 0.3
10	93.2	450	24 ± 0.9	713 ± 48	4.1 ± 0.3
20	99.7	466	24 ± 2.8	1003 ± 94	4.4 ± 0.2
30	99.4	484	24 ± 0.7	1089 ± 152	5.3 ± 0.5

From Table 1, it can be seen that ZrB_2 with 30 vol% SiC would be a good candidate for excellent thermal ablation, thermal shock, and oxidation resistance at ultra high temperatures. Densification is needed to prepare the material to achieve the desired mechanical properties. Figure 1 is an SEM image showing the microstructure of ZrB_2 -30 vol% SiC ceramic material prepared by the Ceramic On-Demand Extrusion (CODE) process.

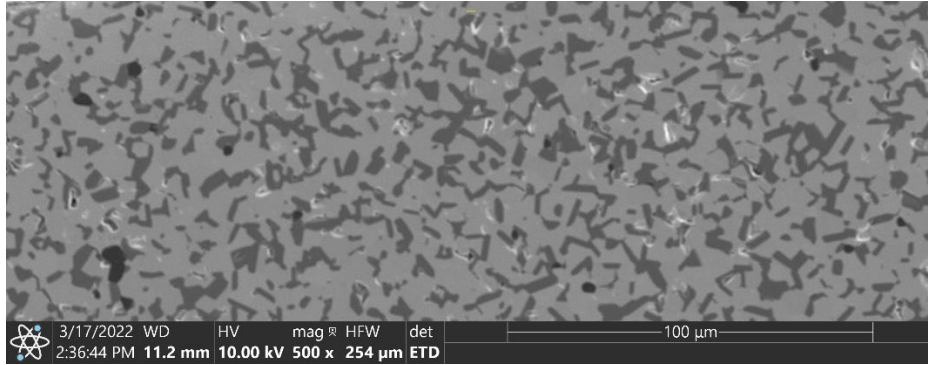


Figure 1: Microstructure of ZrB_2 - SiC (70/30 in vol%) ceramic material by the CODE process

Fabricating the compact heat exchanger by additive manufacturing is one of the promising solutions to overcome the manufacturing challenges while considering ceramic as the build material. The method of producing a desired part layer by layer is known as additive manufacturing [20,21,22]. The Ceramic On-Demand Extrusion process (CODE), with the constructed machine shown in Figure 2, is a freeform extrusion fabrication process developed at the Missouri University of Science and Technology [19, 20] for producing dense ceramic components. An aqueous paste made of ceramic materials with a very low binder content is used as the printing material in this process. A nozzle attached to the extruder is used to print the desired part geometry layer by layer. The paste is extruded from the nozzle using an auger extruder. The auger extruder uses a syringe in which a material pressurized by compressed air is connected as a barrel. This preloaded pressure is required to deliver the paste to the auger chamber and maintain a continuous flow of the paste. Extrusion is performed by rotating the auger using a servo motor. The flow rate is controlled by adjusting the auger’s angular velocity. By maintaining a constant rotation speed of the motor, a constant extrusion rate is achieved.

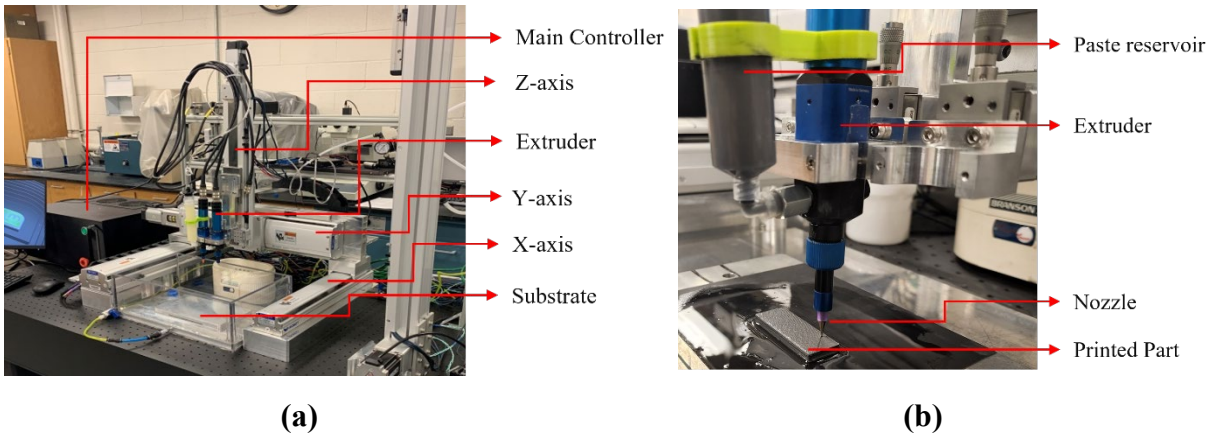


Figure 2: The Ceramic On-Demand Extrusion (CODE) machine

The objective of the current study is to fabricate microchannels with a channel diameter of 500 μm by the CODE process with $\text{ZrB}_2\text{-SiC}$ (70/30 in vol%) material for ultra-high temperature compact heat exchangers. An aqueous paste of $\text{ZrB}_2\text{-SiC}$ is developed with high solid loading that is suitable for printing via the extrusion process. Mechanical properties of the printed samples with this paste are measured, and the printed parts with microchannels are analyzed.

2. Experimental Procedure

2.1. Paste Preparation

The preparation of the paste for extrusion and maintaining its consistency is important since a little amount of fluctuation can change the properties of the paste substantially. The paste for the extrusion contains ZrB_2 powder, SiC powder, DARVAN[®] 821A (Ammonium polyacrylate, Vanderbilt Minerals LLC, Gouverneur, NY), Methocel (Methylcellulose, Dow Chemical Co., Pevely, MO) and deionized (DI) water. The ZrB_2 powder has the particle size of 1.5 - 3.0 microns and the SiC powder has an average particle size of 0.65 microns (according to the manufacturer).

At first, attrition milling is performed on the ZrB_2 and SiC powder particles to mechanically reduce the particle size by milling in coarse milling media with higher rpm. After that, rotovaping is performed to evaporate all the acetone from the powder that is added in the attrition milling procedure. Batches of ceramic paste are produced by mixing 45 vol% $\text{ZrB}_2\text{-SiC}$ milled powder, DARVAN[®] 821A as a dispersant agent, and DI water. The mixture is then ball-milled for 24 hours to prepare a homogenous slurry. Methocel is added as a binder in the slurry through a planetary mixer and left for 8 hours to increase the slurry's density and viscosity into a paste. A syringe charger, THINKY [ARC-40H], is used to load the prepared paste in a syringe which is then attached to the extruder of the CODE machine.

2.2 Fabrication of Microchannels for Compact Heat Exchanger

Computer-aided design models are made with the desired geometry of the heat exchanger. The primary attempt is to print a heat exchanger with 2x2 channels and to collect data for optimization of paste quality and printing parameters. Parts with 10x3 and 30x3 microchannels are printed, with the diameter of each channel being 500 μm and the channel length being 50 mm. The surface area density of the 30x3 part is 390 m^2/m^3 . The CAD images are shown in Figure 3.

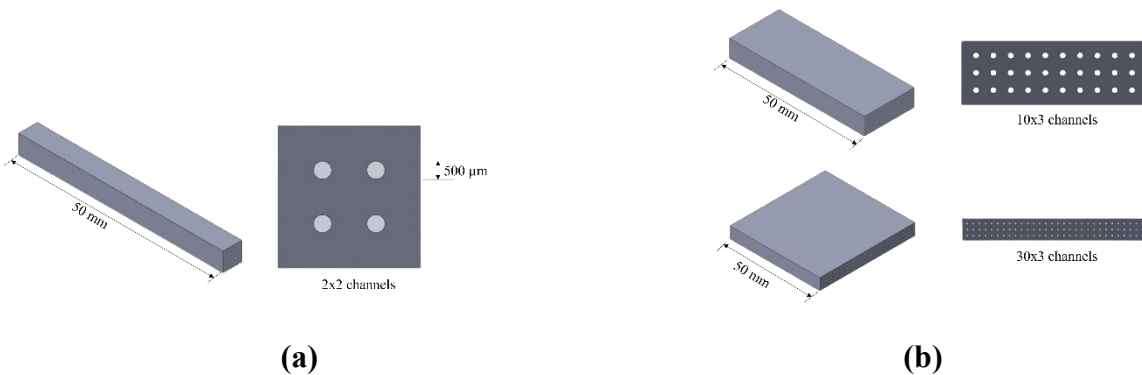


Figure 3: Computer-aided designs of printed specimens: (a) 2x2 channels and (b) 10x3 and 30x3 channels.

The generated CAD file is converted into .stl format, which is then transferred into a slicing software to convert the three-dimensional geometry into multiple layers for the extrusion process to print the specimens layer by layer. The layers then are turned into G-code to create toolpaths for the extruder to follow during printing.

Creating microchannels is the most challenging part of printing a compact heat exchanger because of the compact size and good precision needed. The printing parameters such as printing speed, layer height, and line width need to be optimized in order to achieve microchannels of the desired shape and diameter.

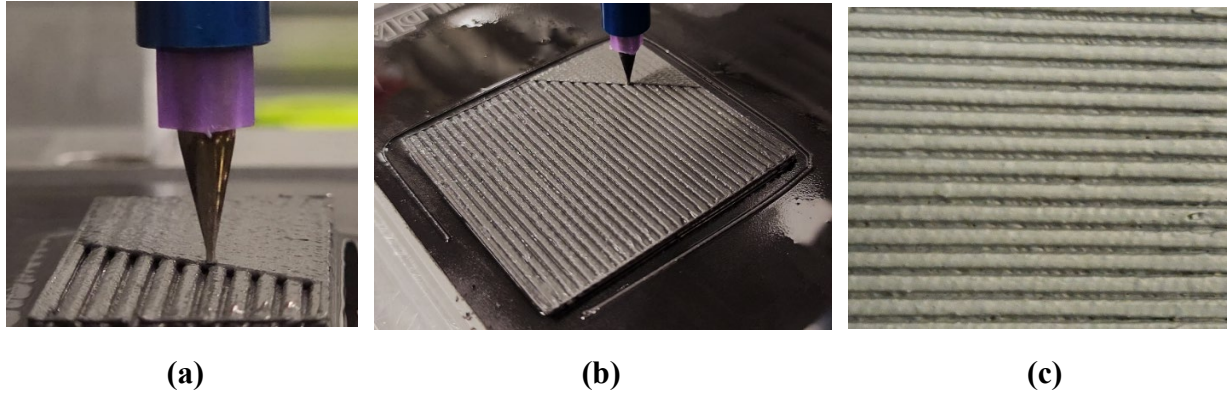


Figure 4: Printing microchannels (a) a 10x3 part being printed, (b) a 30x3 part being printed, (c) top view of printed microchannels

2.3 Post-Processing of Printed Samples

After the parts are printed, post-processing steps including bulk drying, binder burnout, and sintering are needed. Bulk drying is done by putting the printed parts in an environmental chamber with controlled humidity (75%) and temperature (25°C) for 12 hours. By keeping the drying chamber's humidity high and the part's drying rate low, warpage and crack formation are prevented, resulting in the production of crack-free green parts. The printed part is easily detached from the substrate after bulk drying.

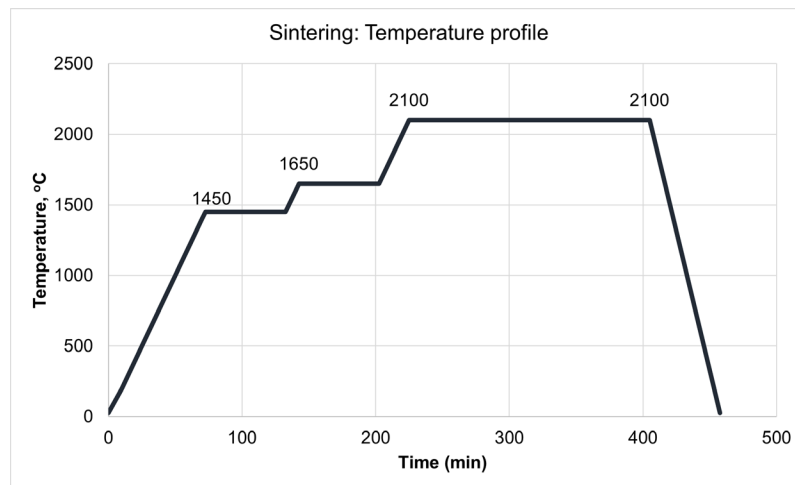


Figure 5: Sintering profile of the printed parts

The binder burnout process is performed in a small retort furnace (Lindberg, St. Watertown, WI) under flowing argon with a heating rate of 5 °C/min to the temperatures of 100, 225, 275, 310, 370, 500, and 600 °C, with a hold of one hour at each temperature before cooling down to room temperature at 10 °C/min. Conventional pressureless sintering in a graphite furnace (Thermal Technology Inc., MODEL#1000-4560-FP30) is done for full densification of the printed ZrB₂-SiC parts. As shown in Figure 5, the furnace is run under vacuum at the rate of 20 °C/min to 1450 °C and 1650 °C with a 1-hour hold at each temperature. After the 1-hour hold at 1650 °C, the densification process occurs at flowing argon gas, and the temperature run up to 2100 °C with a 3-hour hold. After this last hold, the samples are cooled in argon to room temperature at the cooling rate of 40 °C/min.

2.4 Characterization of Sintered Samples

The density of sintered samples is measured by the Archimedes method, with water as the submersion medium according to ASTM Standard C373. The dry mass is measured for each specimen, and the samples are then saturated by being immersed in distilled water and kept under vacuum for 12 hours. The bulk density is then calculated by using the saturated and suspended masses. The relative density of the specimen is calculated by dividing the bulk density by the theoretical density.

Scanning electron microscopy data are collected by using the TFS ESEM Prisma with Pathfinder EDS, WDS, and EBSD. Prior to the SEM imaging, selection of sectioning, mounting to epoxy, grinding, and polishing of the cross-sections of samples (without etching) are performed. The SEM images are analyzed using ImageJ software (Image J 1.53n, United States National Institute of Health, Bethesda, MD).

3. Results and Discussion

The mechanical properties of the sintered samples are determined, and the quality of the printed microchannels is analyzed. Figure 6(a) shows a sintered part with 10x3 microchannels and Figure 6(b) shows the cross-section of a part with 20x2 microchannels, where the microchannels are clearly visible.

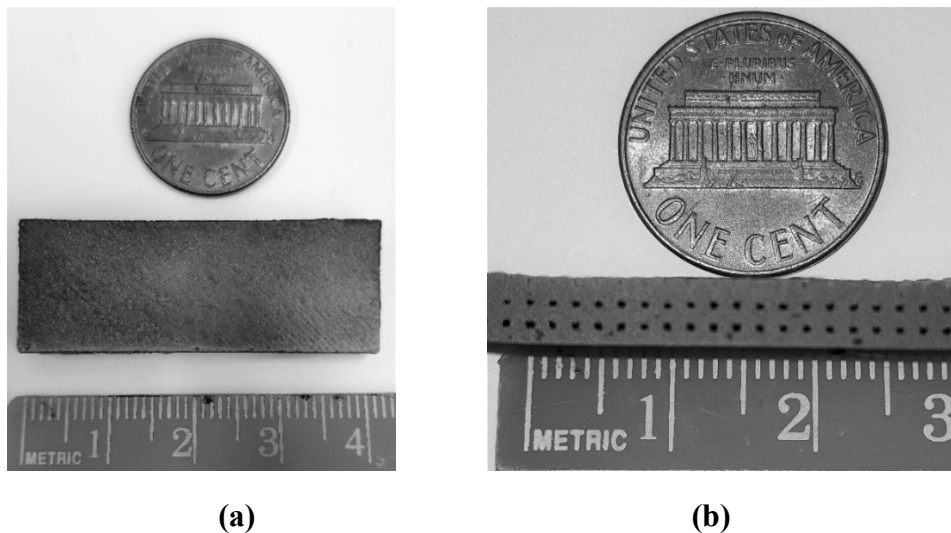


Figure 6: Sintered final parts with microchannels: (a) a sample with 10x3 microchannels, and (b) cross-sectional view of a 20x2 sample

Table 2: Mechanical properties of ZrB₂ – 30 vol% SiC samples

	Flexural Strength (MPa)	Young's Modulus (GPa)	Relative Density (%)
ZrB ₂ -SiC (70/30)	270 ± 42	482 ± 20	96

Table 2 contains the mechanical properties of the printed parts with ZrB₂ – 30 vol% SiC paste. The properties are measured in the printed samples without microchannels. ASTM Standard C1161, with standard type A bars of 2.0 mm x 1.5 mm x 25 mm placed in a screw-driven test frame (model 5881, Instron, Norwood, MA) to determine the properties. The preliminary measurements are conducted with 10 sample bars. The relative density has been measured by the Archimedes method, with water as the submersion medium according to the ASTM Standard C373. The relative density is comparatively lower than the hot-pressed samples shown in Table 1. However, Young's modulus is similar to that of the hot-pressed samples. The process parameters can be optimized by improving the homogeneity of the paste with higher quality shear mixing procedure during paste making. From a printed green part to a sintered part, the part goes through shrinkage in all three principal dimensions, i.e., along the X-axis (length), Y-axis (width), and Z-axis (height) in Figure 2. The shrinkage rates are measured for the sintered parts with microchannels and the average of shrinkage rates in width, length, and height are given in Table 3.

Table 3: The average shrinkage rates of the sintered parts with microchannels

	Linear Shrinkage Rate (%)			Volumetric Shrinkage
	Width	Length	Height	
Sintered ZrB ₂ -SiC sample	19.01%	19.78%	22%	49.5%

SEM micrographs shown in Figure 6 represent the microstructure of some sintered samples with microchannels. Some small pores were observed, which is expected based on the density measurements. The mean cross-sectional area of microchannels calculated is 197,742 μm², which is essentially the same as the nominal cross-sectional area of 196,350 μm². The standard deviation calculated is 27,419 μm².

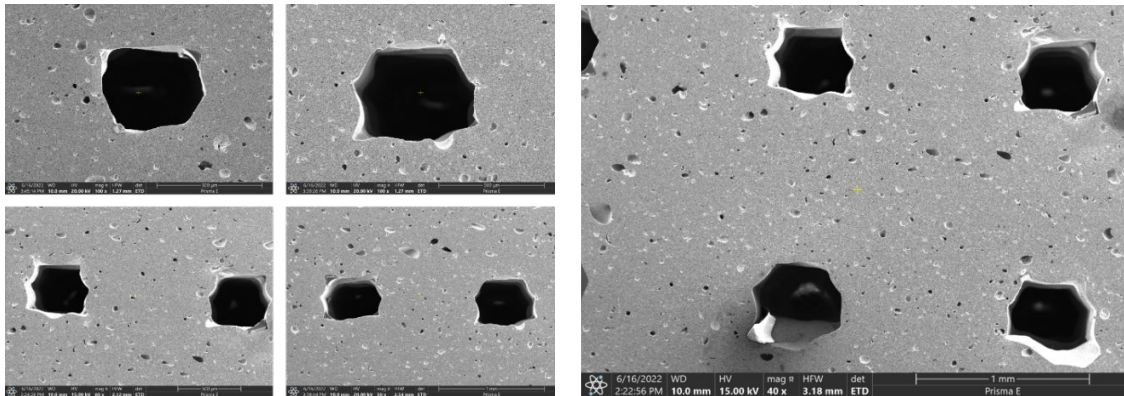


Figure 7: SEM micrograph showing the cross-sectional views of various microchannels

From Figure 7, it is clearly visible that the cross sections of the microchannels are not circular in shape. This demonstrates that creating circular microchannels by an extrusion-based 3D printing method is a major challenge because of the extremely small channel diameter and also the staircase effect of layered printing. We are confident that significant improvement in creating circular microchannels is possible by using a smaller nozzle diameter. However, associated with the reduction of nozzle diameter could be a large increase in the printing time because cutting the nozzle diameter by one half will require quadruple in the printing time. This is a necessary trade-off between part accuracy and printing time. Using a fugitive material to fill in the microchannels and removing the fugitive material in the post-processing may also help making the microchannels more circular. These tests for increasing part shape fidelity will be included in our future study.

The continuity inside each channel is also a major concern for heat exchangers. The channel should be entirely clear throughout the whole channel length. The continuity of the microchannels is also tested for the printed parts. Printed samples are cut into multiple parts across the width and light is transferred from one end to the other end of each sample. There is no blockage inside the channels as shown in Figure 8. The pictures may not give the exact geometrical shape of the microchannels cross-section due to possible misalignment during EDM cutting. For parts with larger dimensions, there is a possibility that a few numbers of channels can get blocked due to uneven drying between each layer and surface warping.

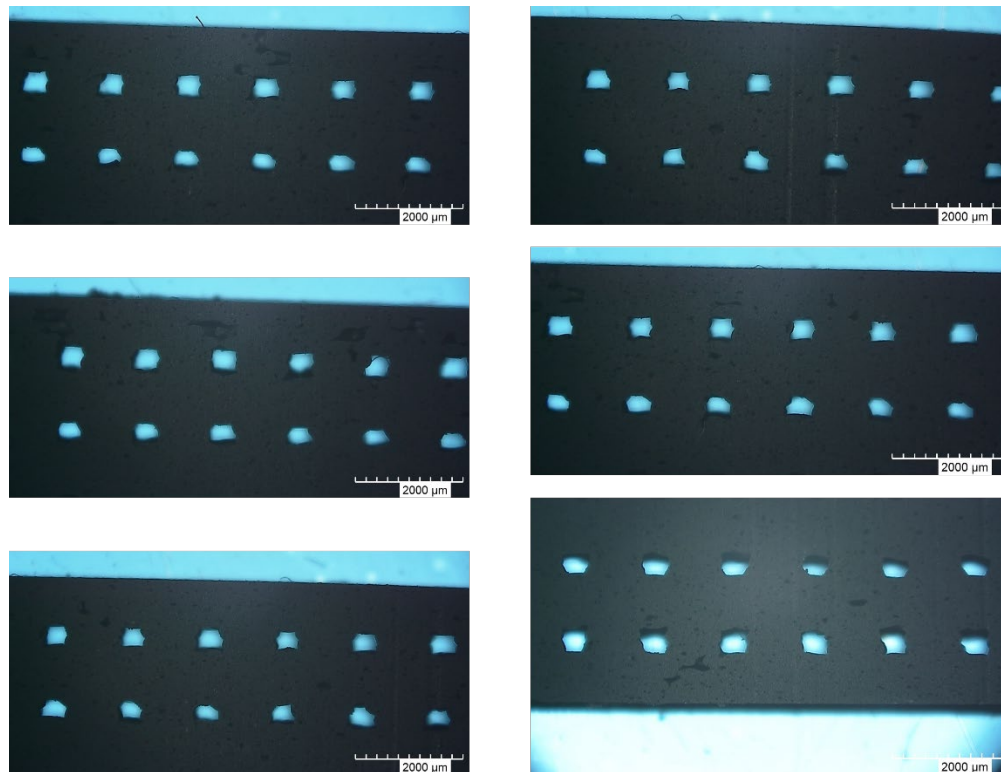


Figure 8: Testing of continuity in microchannels by using an optical microscope

4. Conclusions

An aqueous paste of 70 vol% ZrB₂ – 30 vol% SiC is developed and the Ceramic On-Demand Extrusion (CODE) process is used to fabricate microchannels for the ultra-high temperature ceramic heat exchanger. The paste is prepared with solid loadings of 45 vol%, which shows a promising outcome for use in the 3D printing process. The relative density of the final (sintered) parts is comparatively lower than the parts prepared by the hot-press method, though Young's modulus is similar to that of the hot-pressed samples. Microchannels that are 500 μm in diameter are fabricated, followed by the post-processing steps of bulk drying, debinding and sintering. The optical microscope observation of various cross sections cut from the printed samples confirms the continuity inside the printed microchannels. The shrinkage rates of the final parts are measured to be 19-22% in the width, length, and height directions. The cross-sectional shape of the microchannels is not nearly circular. The shape fidelity can be improved significantly by using nozzles of smaller diameters, but with the trade-off of increased printing time. Using a fugitive material may also possible improve the microchannel fidelity.

Acknowledgments

The information, data, or work presented herein was funded in part by the Advanced Research Projects Agency-Energy (ARPA-E), U.S. Department of Energy, under Award Number DE-AR0001125. The views and opinions of the authors expressed herein do not necessarily state or reflect those of the United States Government or any agency thereof.

References

1. Manente, G., & Fortuna, F. M. (2019). Supercritical CO₂ power cycles for waste heat recovery: A systematic comparison between traditional and novel layouts with dual expansion. *Energy Conversion and Management*, *197*, 111777. <https://doi.org/10.1016/j.enconman.2019.111777>
2. Kim, Y. M., Sohn, J. L., & Yoon, E. S. (2017). Supercritical co₂ rankine cycles for waste heat recovery from Gas Turbine. *Energy*, *118*, 893–905. <https://doi.org/10.1016/j.energy.2016.10.106>
3. Liu, M., Zhang, X., Yang, K., Ma, Y., & Yan, J. (2019). Optimization and comparison on supercritical CO₂ Power Cycles integrated within coal-fired power plants considering the hot and cold end characteristics. *Energy Conversion and Management*, *195*, 854–865. <https://doi.org/10.1016/j.enconman.2019.05.077>
4. Novales, D., Erkoreka, A., De la Peña, V., & Herrazti, B. (2019). Sensitivity Analysis of Supercritical CO₂ Power Cycle Energy and Exergy efficiencies regarding cycle component efficiencies for concentrating solar power. *Energy Conversion and Management*, *182*, 430–450. <https://doi.org/10.1016/j.enconman.2018.12.016>
5. Bae, S. J., Ahn, Y., Lee, J., & Lee, J. I. (2014). Various supercritical carbon dioxide cycle layouts study for molten carbonate fuel cell application. *Journal of Power Sources*, *270*, 608–618. <https://doi.org/10.1016/j.jpowsour.2014.07.121>
6. Jokar, M. A., Ahmadi, M. H., Sharifpur, M., Meyer, J. P., Pourfayaz, F., & Ming, T. (2017). Thermodynamic evaluation and multi-objective optimization of molten carbonate

- fuel cell-supercritical CO₂ brayton cycle hybrid system. *Energy Conversion and Management*, 153, 538–556. <https://doi.org/10.1016/j.enconman.2017.10.027>
7. Bai, W., Zhang, Y., Yang, Y., Li, H., & Yao, M. (2018). 300 MW boiler design study for coal-fired Supercritical CO₂ Brayton Cycle. *Applied Thermal Engineering*, 135, 66–73. <https://doi.org/10.1016/j.applthermaleng.2018.01.110>
 8. Zhou, J., Zhang, C., Su, S., Wang, Y., Hu, S., Liu, L., Ling, P., Zhong, W., & Xiang, J. (2018). Exergy analysis of a 1000 MW single reheat supercritical CO₂ Brayton Cycle coal-fired power plant. *Energy Conversion and Management*, 173, 348–358. <https://doi.org/10.1016/j.enconman.2018.07.096>
 9. Son, S., Heo, J. Y., Kim, N. I., Jamal, A., & Lee, J. I. (2019). Reduction of CO₂ emission for solar power backup by direct integration of Oxy-combustion supercritical CO₂ Power Cycle with Concentrated Solar Power. *Energy Conversion and Management*, 201, 112161. <https://doi.org/10.1016/j.enconman.2019.112161>
 10. Chen, Y., Ma, G., Wang, H., Li, T., & Wang, Y. (2019). Application of carbon dioxide as working fluid in geothermal development considering a complex fractured system. *Energy Conversion and Management*, 180, 1055–1067. <https://doi.org/10.1016/j.enconman.2018.11.046>
 11. Dostal, V., Hejzlar, P., & Driscoll, M. J. (2006). High-performance supercritical carbon dioxide cycle for next-generation nuclear reactors. *Nuclear Technology*, 154(3), 265–282. <https://doi.org/10.13182/nt154-265>
 12. Kim, S. G., Yu, H., Moon, J., Baik, S., Kim, Y., Jeong, Y. H., & Lee, J. I. (2016). A concept design of supercritical CO₂ cooled SMR operating at isolated microgrid region. *International Journal of Energy Research*, 41(4), 512–525. <https://doi.org/10.1002/er.3633>
 13. Ahn, Y., Bae, S. J., Kim, M., Cho, S. K., Baik, S., Lee, J. I., & Cha, J. E. (2015). Review of Supercritical CO₂ Power Cycle Technology and current status of Research and Development. *Nuclear Engineering and Technology*, 47(6), 647–661. <https://doi.org/10.1016/j.net.2015.06.009>
 14. Shah RK. (1981), Classification of heat exchangers, in heat exchangers: thermal-hydraulic fundamentals and design. *Washington, DC: Hemisphere Publishing*, 9–46.
 15. Rohsenow W.M., Hartnett J.P., Cho Y.I., (1998). Handbook of heat transfer. *New York: McGraw-Hill*, 17.1–2.
 16. Li, Q., Flamant, G., Yuan, X., Neveu, P., & Luo, L. (2011). Compact heat exchangers: A review and future applications for a new generation of high temperature solar receivers. *Renewable and Sustainable Energy Reviews*, 15(9), 4855–4875. <https://doi.org/10.1016/j.rser.2011.07.066>
 17. Chamberlain, A. L., Fahrenholtz, W. G., Hilmas, G. E., & Ellerby, D. T. (2004). High-strength zirconium diboride-based ceramics. *Journal of the American Ceramic Society*, 87(6), 1170–1172. <https://doi.org/10.1111/j.1551-2916.2004.01170.x>
 18. Zhang, S. C., Hilmas, G. E., & Fahrenholtz, W. G. (2007). Pressureless Sintering of ZrB₂-SiC Ceramics. *Journal of the American Ceramic Society*, 91(1), 26–32. <https://doi.org/10.1111/j.1551-2916.2007.02006.x>
 19. Li, W., Ghazanfari, A., Leu, M. C., & Landers, R. G. (2017). Extrusion-on-demand methods for high solids loading ceramic paste in freeform extrusion fabrication. *Virtual and Physical Prototyping*, 12(3), 193–205. <https://doi.org/10.1080/17452759.2017.1312735>

20. Ghazanfari, A., Li, W., Leu, M. C., & Hilmas, G. E. (2017). A novel freeform extrusion fabrication process for producing solid ceramic components with uniform layered radiation drying. *Additive Manufacturing*, 15, 102–112. <https://doi.org/10.1016/j.addma.2017.04.001>
21. Sehat, M. H., & Mahdianikhotbesara, A. (2021). Powder spreading in laser-powder bed fusion process. *Granular Matter*, 23(4). <https://doi.org/10.1007/s10035-021-01162-x>
22. Turk, T., Hung, C.H. & Sehat, M.H. (2021). Methods of Automating the Laser-Foil-Printing Additive Manufacturing Process. *International Solid Freeform Fabrication Symposium*, University of Texas at Austin. <https://dx.doi.org/10.26153/tsw/17633>